Extremum-Seeking-Based Fluctuation Mitigation by E×B Actuation in HELCAT

Qiaoqiao Wang, Eugenio Schuster, Mark Gilmore, Shuangwei Xie, Andrew Ware

***Abstract*— We investigate active control of fluctuations via manipulation of flow profiles in a magnetized laboratory plasma device (HELCAT). Fluctuations and particle transport are monitored by electrostatic probes, and $E \times B$ flow profiles controlled via biased ring electrodes. A non-model-based optimization algorithm is implemented to seek control inputs that minimize a cost function related to the fluctuation amplitude. The algorithm is also able to identify radial poloidal flow profiles associated with specific levels of RMS fluctuations.**

I. Introduction

Turbulence, and turbulence-driven transport are ubiquitous in magnetically confined plasmas, where there is an intimate relationship between turbulence, transport, destabilizing mechanisms like gradients, and stabilizing mechanisms like flow shear. Though many of the detailed physics of the interrelationship between turbulence, transport and flow remain unclear, there is clear experimental evidence in both fusion and laboratory plasmas that transport and/or turbulence can be suppressed or reduced via shaping of plasma flow profiles (flow shear), e.g., [1], [2]. Several theories were proposed to explain this phenomenon. Currently, the most accepted cause for transport mitigation is the reduction and/or stabilization of turbulence by sheared $E \times B$ flows.

We investigate active control of fluctuations, including fully developed turbulence and the associated cross-field particle transport, via manipulation of flow profiles in a magnetized laboratory plasma device. Fluctuations and particle transport are monitored by an array of electrostatic probes, and $E \times B$ flow profiles controlled via a set of biased concentric ring electrodes that terminate the plasma column in the linear HELCAT (HELicon-CAThode) plasma device [3] (Fig. 1). The ultimate goal is to establish the feasibility of using advanced active control algorithms to control cross-field turbulence-driven particle transport through appropriate manipulation of radial plasma flow profiles.

We report in this paper the work carried out towards the solution of an open-loop optimal control problem where control laws for the bias ring voltages are sought to minimize a cost functional related to the RMS fluctuation amplitude. Among many optimization techniques that may be considered, Extremum Seeking [4] has been chosen to address this problem since this technique can be applied directly to the plant in real-time without the need of using any dynamic model. This is critical in this application, where the predictions by available models still differ significantly from experimental observations.

This work was supported by the National Science Foundation CAREER award program (ECCS-0645086) and the US Department of Energy (DE-FG02-09ER55022)

Q. Wang and E. Schuster (schuster@lehigh.edu) are with the Department of Mechanical Engineering and Mechanics, Lehigh University, 19 Memorial Drive West, Bethlehem, PA 18015-0385,USA. M. Gilmore and S. Xie are with the Department of Electrical Engineering, University of New Mexico. A. Ware is with the Department of Physics and Astronomy, University of Montana.

Fig. 1. The HELCAT device at University of New Mexico.

When implemented both in the experiment and in a predictive simulation code, the extremum seeking algorithm can not only determine the feedforward or open-loop control signals that minimize fluctuations but also help to identify those radial plasma flow profiles associated with low RMS fluctuation amplitudes. The long-term goal is to develop model-based feedback controllers to regulate the radial plasma flow profiles around these desired low-RMS-fluctuation profiles.

The paper is organized as follows. The HELCAT plasma device is described in Section II. The dynamic model implemented in the predictive code used for the tuning of the extremum seeking algorithm is summarized in Section III. The basis of the extremum seeking algorithm is introduced in Section IV. Experimental results are presented in Section V. The paper is closed by the conclusion and future work statement in Section VI.

II. The HELCAT Plasma Device

The HELCAT (Helicon-Cathode) linear plasma device at University of New Mexico (UNM) [3], shown in Fig. 1, consists of a 4 m long, 50 cm diameter cylindrical stainless steel vacuum chamber in two 2 m sections. Each section has eight 10 in, twelve 8 in, and fourteen 3.375 in conflat type ports providing excellent diagnostic access. Currently four 10 in gate valves and seven KF-40 differentially pumped linear probe feedthroughs provide diagnostic access while under vacuum. Magnetic fields are produced by a total of

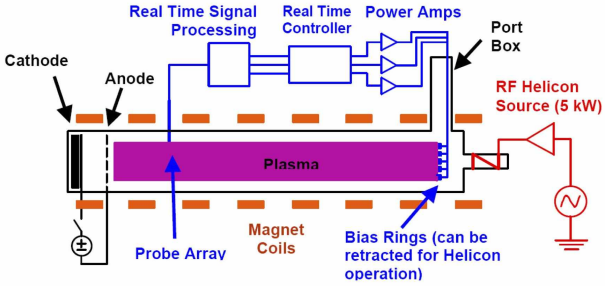

Fig. 2. Schematic of HELCAT feedback control system.

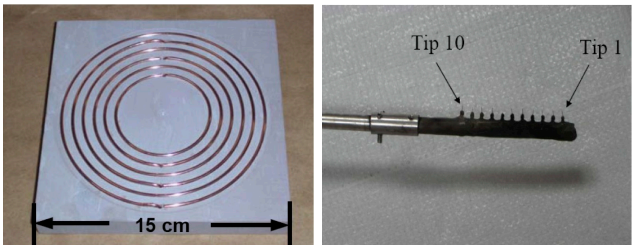

Fig. 3. Left: Copper concentric bias rings mounted on ceramic substrate. Ring radii are: 3.0, 3.7, 4.4, 5.1, 5.9, and 6.6 cm. Right: Multi-point probe.

thirteen water-cooled solenoidal magnetic coils (steady state magnetic fields of up to 2.2 kG at 500 A).

The vacuum chamber has a helicon RF source on one end and a thermionic cathode on the other. Each source can be operated independently, or both sources can be operated simultaneously. Using both sources, HELCAT is capable of operating over a wide range of plasma collisionalities (via changes in background neutral pressure).

The schematic in Fig. 2 shows a typical hardware configuration used for real-time measurement and control. The feedback control system makes use of the concentric bias rings that terminate the plasma column to manipulate the $E \times B$ flow profiles. Fig. 3 (left) shows a realization of a set of 6 copper rings, spaced $\sim$7 mm center-to-center, mounted on a ceramic substrate. HelCat has an extensive and growing suite of plasma diagnostics. Fig. 3 (right) shows a typical multi-point or "rake" probe.

III. Dynamic Model

Based on [5], the transport model under development for HELCAT follows the one-dimensional (radial, r) evolution of the axially averaged density, $n(r,t)$, electron temperature, $T_e(r,t)$, ion temperature, $T_i(r,t)$, poloidal flow, $V_\theta(r,t)$, radial electric field, $E_r(r,t)$, and RMS fluctuation amplitude, $\varepsilon(r,t)$.

The evolution equation for the density is

$$\frac{\partial n}{\partial t} = S + \frac{1}{r}\frac{\partial}{\partial r}\left[rD_n\frac{\partial n}{\partial r}\right], \tag{1}$$

where $D_n = D_{\text{neo}} + D_\varepsilon \varepsilon^2$ is the total particle diffusivity, which includes both neoclassical and turbulent effects. D_{neo} and D_ε are constants, and S is the helicon/cathode particle source, which is modeled by a flat-top radial profile (r_0 is the radial width of the source.), i.e.,

$$S(r) = \begin{cases} S_0, & r \le r_0 \\ 0, & r > r_0 \end{cases}. \tag{2}$$

The electron temperature (energy) equation is

$$\frac{3}{2}\frac{\partial nT_e}{\partial t} = P_e + \frac{1}{r}\frac{\partial}{\partial r}\left[r\left(D_{Te}n\frac{\partial T_e}{\partial r} + \frac{5}{2}D_nT_e\frac{\partial n}{\partial r}\right)\right] + D_n\frac{1}{n}\frac{\partial n}{\partial r}\frac{\partial nT_i}{\partial r} - qb\sqrt{\frac{1}{T_e}}n^2\left(1 - \frac{T_{i0}T_i}{T_{e0}T_e}\right), \tag{3}$$

where $P_e = SE_{e0}$ is the electron power source and E_{e0} is the source energy for electrons. The second and third terms on the right hand side of the equation are related to diffusive energy transport, while the last term represents the ion-electron energy transfer. The electron temperature normalization factor, T_{e0}, the ion temperature normalization factor, T_{i0}, the electron thermal diffusivity, D_{Te} and the ion-electron energy exchange factor, qb, are all constant.

The ion temperature (energy) equation is

$$\frac{3}{2}\frac{\partial nT_i}{\partial t} = P_i + \frac{1}{r}\frac{\partial}{\partial r}\left[r\left(D_{Ti}n\frac{\partial T_i}{\partial r} + \frac{5}{2}D_nT_i\frac{\partial n}{\partial r}\right)\right] - D_n\frac{1}{n}\frac{\partial n}{\partial r}\frac{\partial nT_i}{\partial r} + qb\sqrt{\frac{1}{T_e}}n^2\frac{T_{e0}}{T_{i0}}\left(1 - \frac{T_{i0}T_i}{T_{e0}T_e}\right) - \mu nT_i, \tag{4}$$

where $P_i = SE_{i0}$ is the ion power source and E_{i0} is the source energy for ions. The second and third terms on the right hand side of the equation are related to diffusive energy transport, the fourth term represents the ion-electron energy transfer, while the last term denotes the charge-exchange damping. The charge-exchange damping coefficient μ is constant.

The poloidal, or azimuthal, flow equation is

$$\frac{\partial V_\theta}{\partial t} = -\mu_\theta V_\theta + \alpha_\theta\frac{1}{r^2}\frac{\partial}{\partial r}\left[r^2\left(\frac{\partial \varepsilon^2}{\partial r}\right)\left(\frac{\partial E_r}{\partial r}\right)\right] + \frac{1}{r}\frac{\partial}{\partial r}\left(rD_{V_\theta}\frac{\partial V_\theta}{\partial r}\right) + \tau_\theta, \tag{5}$$

where μ_θ is the coefficient of magnetic damping, α_θ is the coefficient of Reynolds stress flow generation, D_{V_θ} is the poloidal momentum diffusion coefficients, and τ_θ is an external momentum source. Excluding the external momentum source effect, the generation of flow is a competition between the Reynolds stress flow drive and both magnetic damping and momentum diffusion.

The radial electric field is determined by ion force balance,

$$E_r = -B_\phi V_\theta + \alpha\left(\frac{dT_i}{dr} + \frac{T_i}{n}\frac{dn}{dr}\right), \tag{6}$$

where B_ϕ is the axial component of the magnetic field and α is a constant. With the low ion pressure found in the experiment, poloidal flow is likely to be the dominant contribution to the radial electric field.

Finally, the evolution of the RMS fluctuation is given by

$$\frac{\partial \varepsilon}{\partial t} = \left\{\gamma_0 T_e\left(\frac{1}{n}\frac{\partial n}{\partial r}\right)^2 - \alpha_{\varepsilon 1}\varepsilon\left|\frac{\partial T_e}{T_e\partial r} + \frac{\partial n}{n\partial r}\right|^{-\frac{1}{4}} - \alpha_{\varepsilon 2}\left[r\frac{\partial}{\partial r}\left(\frac{E_r}{r}\right)\right]^2\right\}\varepsilon + \frac{1}{r}\frac{\partial}{\partial r}\left[rD_\varepsilon\frac{\partial \varepsilon}{\partial r}\right], \tag{7}$$

where $\varepsilon \equiv \sqrt{<(\tilde{n}/n)^2>}$ ($\tilde{n}$ is the density fluctuation), γ is the linear growth rate (a function of the density and

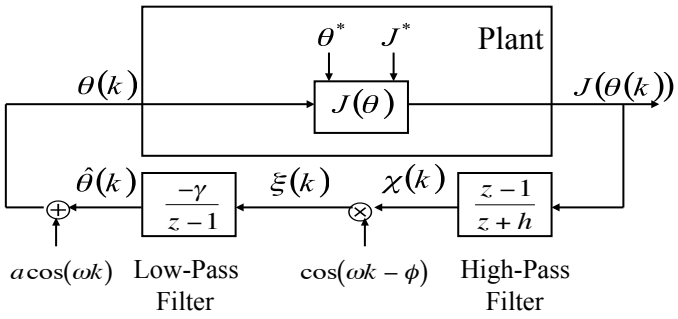

Fig. 4. Extremum seeking control scheme for discrete-time systems.

temperature profiles), $\alpha_{\varepsilon 1}$ is the nonlinear energy transfer coefficient, and $\alpha_{\varepsilon 2}$ is the shear suppression coefficient. The last term on the right hand side of the equation represent the diffusive fluctuation transport. The evolution of the fluctuation envelope is a competition between the linear drive and the various attenuation mechanisms: nonlinear transfer, shear suppression and radial spreading. The growth rate γ model for HELCAT has been developed based on the theory of drift wave instabilities in helicon plasmas [6].

The control elements, biased concentric rings in the experiment, are modeled as localized momentum sources in the transport code (in practice, Gaussian function momentum sources). The effect will be identical to a source of poloidal $E \times B$ flow in the limit of zero β (i.e., when diamagnetic flows are negligible). The external poloidal momentum source from the rings is

$$\tau_\theta(r) = \sum_{i=1}^{6} \tau_{\theta i} e^{\frac{(r-r_i)^2}{2w_i^2}} \tag{8}$$

where the input variable $\tau_{\theta i}$ denote the source strength, r_i represent the radial location and $w(i)$ denotes the width of the Gaussian momentum source for the i-th bias ring ($i = 1, \ldots, 6$). The bias ring locations for HELCAT are 3.0 cm, 3.7 cm, 4.4 cm, 5.1 cm, 5.9 cm, 6.6 cm. The plasma radius is $\sim$8 cm.

IV. Extremum Seeking

A. Fundamentals of Extremum Seeking

Extremum seeking optimal control has found applications in many engineering areas. Extremum seeking is applicable in situations where there is a nonlinearity in the control problem, and the nonlinearity has a local minimum or a maximum. One of the most attractive features of the method is its non-model-based nature, which places it in a privileged position in comparison of model-based optimization methods when the knowledge of the plant is limited. In this work we use extremum seeking for adaptive tuning of the torque source τ in numerical simulations or the bias ring voltages V in the experiment in order to minimize a function related to the RMS fluctuation.

We change θ (torque source τ in numerical simulations or bias ring voltages V in the experiment) after each plasma run, therefore, we employ the discrete time variant of extremum seeking [4], [7]. The implementation is depicted in Fig. 4, where z denotes the Z-transform variable. The static nonlinear block $J(\theta)$ is defined in this case as a measure of the plasma RMS fluctuation. The objective is to minimize J. The variables θ^* and J^* denote respectively the minimizing values of θ and the minimum value of J, i.e., $J^* = J(\theta^*)$. The probing signal, $a\cos(\omega k)$ with $a > 0$, in Fig. 4, fed into the plant helps to get a measure of the gradient of the map $J(\theta)$, which is used to drive the parameters θ to the minimizing values θ^*, and therefore J to its minimum value J^*. We can summarize the extremum seeking algorithm shown in Fig. 4 as

$$\begin{aligned}
\chi(k) &= -h\chi(k-1) + J(k) - J(k-1) && (9)\\
\xi(k) &= \chi(k)\cos(\omega k - \phi) && (10)\\
\hat{\theta}(k+1) &= \hat{\theta}(k) - \gamma\xi(k) && (11)\\
\theta(k+1) &= \hat{\theta}(k+1) + a\cos(\omega(k+1)). && (12)
\end{aligned}$$

The high-pass filter, $\frac{z-1}{z+h}$, is designed as $0 < h < 1$, and the modulation frequency ω is selected such that $\omega = \alpha\pi$, $0 < |\alpha| < 1$, and α is rational. It is important to select ω large in a qualitative sense when compared with the plant time scale. The cut-off frequencies of the filters need to be lower than the frequency ω of the probe signal. These observations impose constraints and, at the same time, a relationship between ω and h. As an additional constraint, ω should not equal any frequency present in the measurement noise. The perturbation amplitude a needs to be small in order to make the steady state output error also small. Given a, the adaptation gain γ of the low pass filter, $\frac{-\gamma}{z-1}$, needs to be small enough to preserve stability. In this case we are dealing with a multi-parameter extremum seeking procedure where each component of the vector θ has its associated a, γ, h, ω and ϕ parameters.

For this application we define the cost function as

$$J = \sum_{i=1}^{4} k_i J_i, \tag{13}$$

where k_i are weighting constants and J_i are functions of the RMS fluctuation ε at different points in space r_i ($i = 1, \ldots, 4$) averaged over a predefined period of time, i.e.,

$$J_i = J_i(\bar{\varepsilon}(r_i, \theta)), \tag{14}$$

where

$$\bar{\varepsilon}(r_i, \theta) = \frac{1}{t_2 - t_1}\int_{t_1}^{t_2} \varepsilon(t, r_i, \theta)dt. \tag{15}$$

In each iteration k of the extremum seeking procedure, or equivalently, in each plasma run, we fix $\theta(k)$ (torque source τ in numerical simulations or bias ring voltages V in the experiment) and obtain direct or indirect time-averaged measurements of the RMS fluctuation at four points in space, i.e., $\bar{\varepsilon}(r_i, \theta(k)))$ for $i = 1, \ldots, 4$. These measurements are used to compute $J(\theta(k))$ as defined in (13)-(14), which is in turn fed into the extremum-seeking algorithm (9)-(12) to compute $\theta(k+1)$.

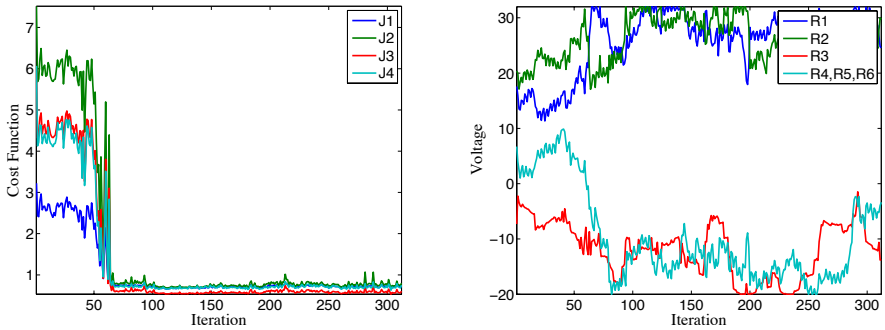

(a) (b)

Fig. 5. (a) Experimental cost function components, (b) Ring voltages (θ).

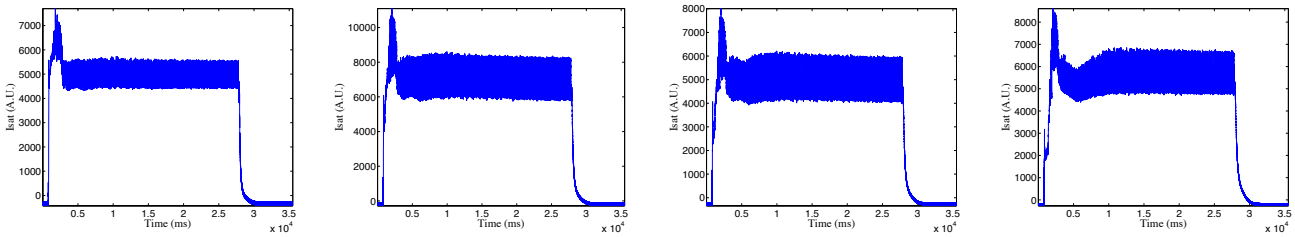

(a) (b) (c) (d)

Fig. 6. Ion saturation current evolution before the extremum seeking controller is turned on: (a) tip 3, (b) tip 5, (c) tip 6, (d) tip 8.

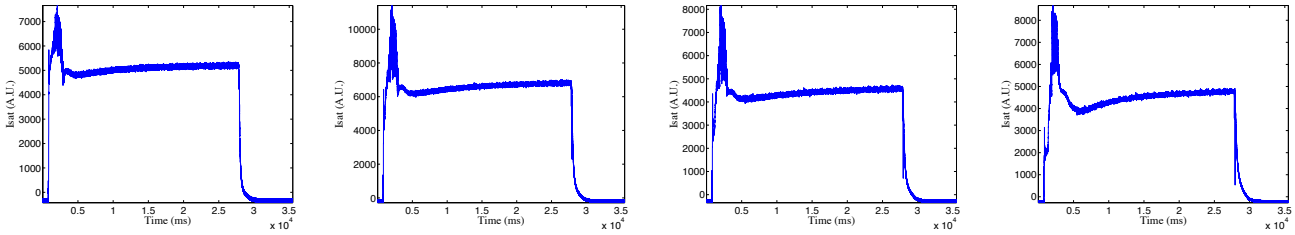

(a) (b) (c) (d)

Fig. 7. Ion saturation current evolution after the extremum seeking controller is turned on: (a) tip 3, (b) tip 5, (c) tip 6, (d) tip 8.

V. Experimental Procedure

A. Experimental Setup

Due to the availability of only four power supplies, the three outer bias rings shown in Fig. 3 (left) have been connected in parallel. Therefore, while the voltages of the three inner rings can be controlled independently, the voltages of the three outer rings can be controlled only as a group. The power suppliers are grounded to the HELCAT chamber and their output ranges are -20V/+20V. Based on experimental observations obtained in a trial and error procedure, the power supplies for the two inner rings have been connected in series with 12 V car batteries in order to improve the efficiency of the bias rings in terms of fluctuation mitigation. The ranges for the two inner power supplies are -8V/+32V. The tips 3, 5, 6 and 8 of the rake probe shown in Fig. 3 (right) have been used to simultaneously obtain fluctuation-related measurements at several points along the plasma radius.

B. Extremum Seeking Setup

The predictive code based on the model (1)-(8) has played a crucial role in tuning up the parameters of the extremum seeking algorithm (9)-(12). The code is still under development and validation but it already provides qualitative predictions that match experimental observations. However, there are two key differences at this moment between the numerical code and the experiment:

1) Although the numerical code can predict the evolution of the RMS envelope of the fluctuation ε based on (7), in the real experiment we can only measure a signal that is proportional to the fluctuation as it will be explained below.
2) While in the numerical code the control inputs are the strengths $\tau_{\theta i}$ of the momentum or torque sources as defined in (8), in the real experiment the control inputs are the voltages of the bias rings. These voltages create an electrical field in the radial direction that by interacting with the axial magnetic field produces torque in the poloidal or azimuthal direction.

In order to emulate the experimental conditions imposed by the availability of four power sources, the to-be-optimized extremum seeking parameters are defined as $\theta_1 = \tau_{\theta 1}$, $\theta_2 = \tau_{\theta 2}$, $\theta_3 = \tau_{\theta 3}$, $\theta_4 = \tau_{\theta 4} = \tau_{\theta 5} = \tau_{\theta 6}$ in the simulations. The cost function (13)-(14) is defined as

$$J_i(\bar{\varepsilon}(r_i, \theta)) = \bar{\varepsilon}(r_i, \theta) \tag{16}$$

with $t_1 = 100$ ms and $t_2 = 250$ ms in (15). The measurement points are chosen as 5 cm, 5.8 cm, 6.2 cm and 7 cm from the plasma center and the simulation time is set to 250 ms. The extremum seeking parameters are tuned as $h = 0.4$, $\omega_i = 0.065i\pi$, for $i = 1, \ldots, 4$, and $\gamma = 0.5$ based on the numerical predictions provided by the code (1)-(8).

C. Experimental Results

We focus in this paper on the experimental results obtained after the implementation in HELCAT of the extremum-seeking algorithm (9)-(12), which was tuned based on numerical simulations carried out based on the code model (1)-(8). For the experiment we define $\theta_1 = V_1$, $\theta_2 = V_2$, $\theta_3 = V_3$, $\theta_4 = V_4$, where V_i, for $i = 1, \ldots, 4$, represent the voltages on the bias rings R_1, R_2, R_3 and $R_4/R_5/R_6$ respectively (R_1 denotes the most inner ring while R_6 denotes the most outer ring). The radii r_i, for $i = 1, \ldots, 4$, denote the positions of the third, fifth, sixth and eighth tips of the rake probe.

1) Fluctuation Mitigation: The first extremum-seeking implementation focused on fluctuation mitigation. The goal in this case is to reduce the fluctuation level and completely suppress it if possible. Therefore, we define the cost function (13)-(14) as

$$J_i(\bar{\varepsilon}(r_i, \theta)) = \bar{I}_s\left(r_i, \theta\right), \tag{17}$$

where we define

$$\bar{I}_s(r_i, \theta) = \frac{1}{t_2 - t_1} \int_{t_1}^{t_2} \sqrt{\tilde{I}_s^2(t, r_i, \theta)} dt \tag{18}$$

$$\tilde{I}_s(t, r_i, \theta) = I_s(t, r_i, \theta) - I_s^o(r_i, \theta) \tag{19}$$

$$I_s^o(r_i, \theta) = \frac{1}{t_2 - t_1} \int_{t_1}^{t_2} I_s(t, r_i, \theta) dt. \tag{20}$$

with $t_1 = 100$ ms and $t_2 = 250$ ms. This time-interval choice is based on the fact that the transient dampens out after 80 ms and the experiment can be consider in quasi steady state for 100 ms $\leq t \leq$ 250 ms. I_s denotes the ion saturation current signal provided by the rake probe, which is proportional to $\sqrt{T_e} n$. If we write $T_e \approx < T_e > + \tilde{T}_e$ and $n \approx < n > + \tilde{n}$, where $<>$ denotes average or 0th order contribution and $\tilde{}$ denotes fluctuation or 1st order contribution, and take into account that the T_e fluctuation is very small compared to its average value, we can conclude that $I_s \propto \sqrt{< T_e >} < n > + \sqrt{< T_e >} \tilde{n}$. This implies that $\tilde{I}_s \propto \tilde{n}$, and therefore $\bar{I}_s$ is an indirect measure of $\bar{\varepsilon}$.

Fig. 5(a) shows the evolutions of the four components $J_i(\bar{\varepsilon}(r_i, \theta)) = \bar{I}_s\left(r_i, \theta\right)$ of the cost function, where r_i, for $i = 1, \ldots, 4$, represent the positions of the tips 3, 5, 6 and 8 of the rake probe, as a function of the extremum seeking iterations, i.e., as a function of the HELCAT plasma discharges. We can note that after 60 discharges the fluctuation is driven to a much lower level than that present before turning on the extremum seeking controller. The evolutions of the components of the extremum-seeking θ parameter, which are the voltages provided by the four power amplifiers, are shown in Fig. 5(b). We can see that the two inner bias ring voltages are driven by the extremum seeking algorithm to positive values around 25V, while the voltages of the four outer bias rings are driven to negative values around -10V. Fig. 6 shows time evolution of the ion saturation current, whose variance is proportional to the density fluctuation, before turning on the extremum-seeking controller at the four spatial locations defined by the positions of the tips 3, 5, 6 and 8 of the rake probe. By comparing Fig. 6(a)-(d), it is possible to note that the fluctuation phenomenon is indeed more severe at the far edge of the plasma. After the extremum-seeking controller is turned on, Fig. 7 shows that the fluctuation levels measured by the four tips of the probe are dramatically reduced. By comparing Fig. 7(a)-(d) we can note that extremum seeking is effective in mitigating fluctuation both at the center and at the edge of the plasma.

2) Fluctuation Regulation: The second extremum-seeking implementation focused on fluctuation regulation. The goal in this case is not to suppress fluctuation but to regulate it around a desired level. Therefore, we define the cost function (13)-(14) as

$$J_i(\bar{\varepsilon}(r_i, \theta)) = \sqrt{\left(\bar{I}_s\left(r_i, \theta\right) - \bar{I}_s^*\left(r_i\right)\right)^2}, \tag{21}$$

where $\bar{I}_s^*$ denotes the desired value of $\bar{I}_s\left(r_i, \theta\right)$, which is related to a desire value for $\bar{\varepsilon}$. We set $\bar{I}_s^*(r_1) = 2$, $\bar{I}_s^*(r_2) = 4$, $\bar{I}_s^*(r_3) = 3$ and $\bar{I}_s^*(r_4) = 3$.

Fig. 8(a) shows the evolutions of $\bar{I}_{si} = \bar{I}_s(r_i)$, where r_i, for $i = 1, \ldots, 4$, represent the positions of the tips 3, 5, 6 and 8 of the rake probe, as a function of the extremum seeking iterations, or equivalently, the HELCAT plasma discharges. We can note that the extremum seeking controller drives $\bar{I}_s(r_1) \rightarrow\sim 2$, $\bar{I}_s(r_2) \rightarrow 3.5$, $\bar{I}_s(r_3) \rightarrow 3.5$ and $\bar{I}_s(r_4) \rightarrow 5$. It is important to emphasize that the desired values $\bar{I}_{si}^*$, for $i = 1, \ldots, 4$, have been chose arbitrarily and there is no guarantee that they are indeed achievable. The evolutions of the components of the extremum-seeking θ parameter, which are the voltages provided by the four power amplifiers, are shown in Fig. 8(b). We can see that the two inner bias ring voltages are driven by the extremum seeking algorithm to positive values around 20V, while the voltages of the four outer bias rings are driven to negative values around -10V. Fig. 9 shows the time evolution of the ion saturation current, whose variance is proportional to the density fluctuation, before turning on the extremum-seeking controller at the four spatial locations defined by the positions of the tips 3, 5, 6 and 8 of the rake probe. After the extremum-seeking controller is turned on, Fig. 10 shows that the fluctuation levels measured by the four tips of the probe are reduced but not suppressed. It is interesting to note the sudden change in the fluctuation level at around 150 ms. This phenomenon needs further exploration but we anticipate that it may be related to the fact that the to-be-minimized cost function is defined in terms of the time average of the fluctuation. The extremum seeking controller seems to drive the voltages to values where this sudden change is possible in order to achieve the time-averaged level of fluctuation specified by $\bar{I}_{si}^*$, for $i = 1, \ldots, 4$. By comparing Fig. 10(a)-(d) we can note that extremum seeking is effective in regulating fluctuation at both the center and the edge of the plasma.

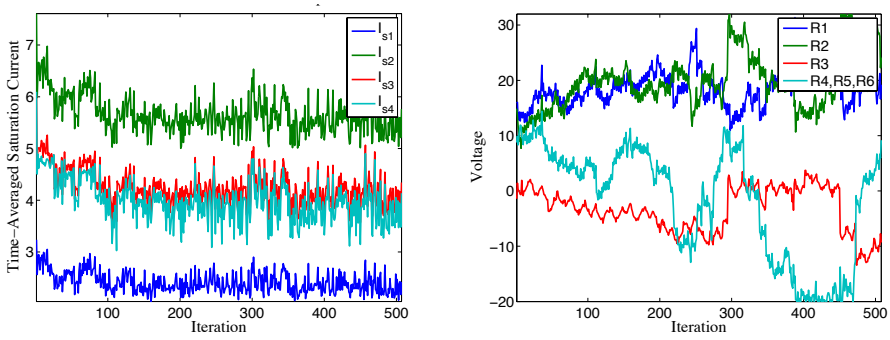

(a) (b)

Fig. 8. (a) Experimental time-averaged ion saturation current components, (b) Ring voltages (θ).

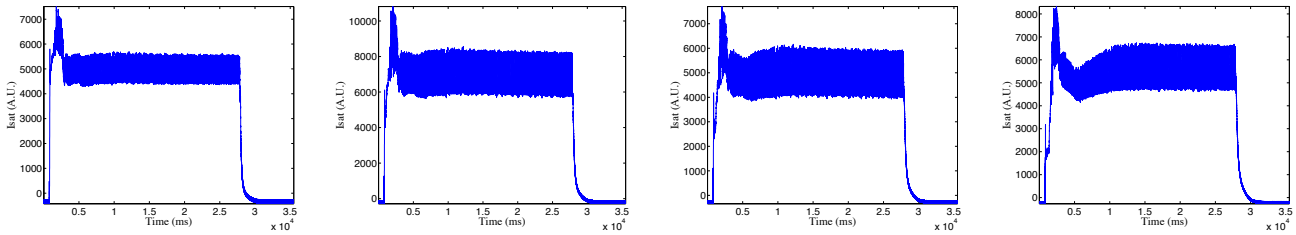

(a) (b) (c) (d)

Fig. 9. Ion saturation current evolution before the extremum seeking controller is turned on: (a) tip 3, (b) tip 5, (c) tip 6, (d) tip 8.

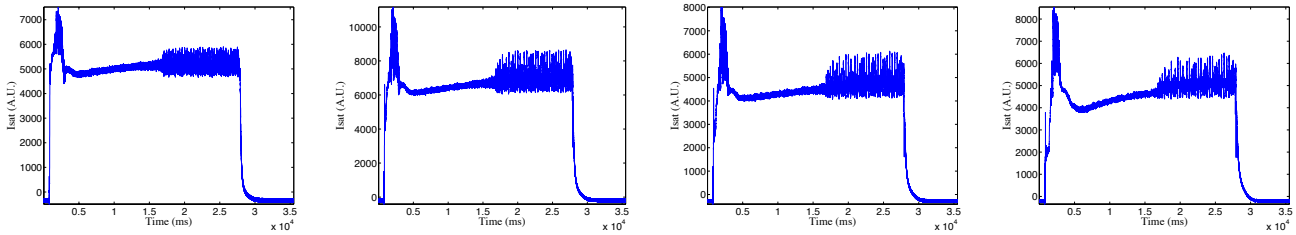

(a) (b) (c) (d)

Fig. 10. Ion saturation current evolution after the extremum seeking controller is turned on: (a) tip 3, (b) tip 5, (c) tip 6, (d) tip 8.

VI. Conclusions

A multi-parameter, extremum-seeking, adaptive controller has been designed for plasma fluctuation mitigation in HELCAT. The controller can successfully regulate the fluctuation level by adaptively tuning the bias ring voltages. The controller's non-model-based nature represents an advantage in this case when compared with other model-based optimization techniques due to the challenges arising in the modeling of the system dynamics. Constraints and competing objectives can be incorporated into the cost function.

The controller has been successfully tuned using a predictive simulation code. Motivated by the promising results obtained in the simulation study, the controller has been implemented in HELCAT, where it has been proved effective in controlling the plasma fluctuation. The controller can fully suppress fluctuation or regulate it around a pre-specified desired value. This capability of the extremum-seeking controller makes it an extremely useful tool for the study of the underlying physics of the system. A multi-point probe capable of simultaneously measuring the poloidal flow at different points along the plasma radius is currently under development. This probe will allow for the identification of the radial poloidal flow profiles associated with specific levels of RMS fluctuation regulated by the extremum-seeking controller and will also enable real-time profile reconstruction and feedback control. This application is a clear example on how advanced control techniques can be used as tools to elucidate the physics of laboratory and fusion plasmas.

References

[1] P. W. Terry, "Suppression of Turbulence and Transport by Sheared Flow," *Reviews of Modern Physics*, vol. 72, no. 1, pp. 109–165, 2000.

[2] N. Crocker, G. Y. Burin, M. J. Burin, G. R. Tynan, B. P. Cluggish, and K. R. Umstadter, "Control of Velocity Shear and Turbulence Through Biasing in CSDX," *Program of the 44th Annual Meeting of the APS Division of Plasma Physics*, vol. 47, p. 264, 2002.

[3] A. G. Lynn, M. Gilmore, C. Watts, J. Herrea, R. Kelly, S. Will, S. Xie, L. Yan, and Y. Zhang, "The HelCat dual-source plasma device," *Review of Scientific Instruments*, vol. 80, no. 103501, 2009.

[4] K. Ariyur and M. Krstic, *Real-Time Optimization by Extremum Seeking Feedback*. Wiley, 2003.

[5] D. E. Newman, B. A. Carreras, D. Lopez-Bruna, P. H. Diamond, and V. B. Lebedev, "Dynamics and control of internal transport barriers in reversed shear discharges," *Physics of Plasmas*, vol. 5, no. 4, pp. 938–952, 1998.

[6] R. F. Ellis, E. Marden-Marshall, and R. Majeski, "Collisional drift instability of a weakly ionized argon plasma," *Plasma Physics*, vol. 22, pp. 113–132, 1980.

[7] K. A. J. Choi, M. Kristic and J. Lee, "Extremum seeking control for discrete-time systems," *IEEE Transactions on Automatic Control*, vol. 47, no. 2, pp. 318–323, 2002.